Int. J. Heat Mass Transfer. Vol. 36, No. 2, pp. 507–517, 1993
Printed in Great Britain

0017-9310/93 $6.00 + 0.00

Simulation and measurement of enhanced turbulent heat transfer in a channel with periodic ribs on one principal wall

TONG-MIIN LIOU,† JENN-JIANG HWANG and SHIH-HUI CHEN
Power Mechanical Engineering Department, National Tsing Hua University, Hsinchu, Taiwan 300, R.O.C.

(*Received* 5 *August* 1991 *and in final form* 27 *December* 1991)

Abstract—This paper performs a numerical and experimental analysis to investigate the heat transfer and fluid flow behavior in a rectangular channel flow with streamwise-periodic ribs mounted on one of the principal walls. The k–ε–A PDM turbulence model together with a smoothed hybrid central/skew upstream difference scheme (SCSUDS) and the PISO pressure–velocity coupling algorithm was applied to solving the accelerated, separated and recirculating flows. The real-time holographic interferometry technique was adopted to measure the time-dependent temperature field in the ribbed duct. The predicted fluid flow and temperature field were tested by previous LDV measurements and present holographic interferometry data, and reasonable agreement was achieved. By the examination of the local wall temperature distribution for the uniform wall heat flux (UHF) boundary condition the regions susceptible to the hot spots are identified. Moreover, the study provided the numerical solution to investigate the effect of geometry and flow parameters on the local as well as average heat transfer coefficients. The compact correlation of the average heat transfer coefficient was further developed and accounted for the rib height, rib spacing, and Reynolds number.

INTRODUCTION

FLOW INTERRUPTION created in flow passages at periodic intervals is a popular means for heat transfer enhancement. This problem is of practical importance and widely considered in the design of devices such as heat exchangers, advanced gas-cooled reactor fuel elements, and electronic cooling devices. The flow passages of these devices are usually roughened only on one principal wall by ribs in a periodic manner along the flow direction, and the fluid flow is characterized as a turbulent flow. The purpose of this paper is to analyze the flow and heat transfer in a streamwise periodic geometry, as shown in Fig. 1. The geometry consists of a parallel plate channel with an array of square ribs positioned transversely to the streamwise direction on the wall.

There are numerous publications in which the effectiveness of the aforementioned augmentation was investigated. The relevant literature about the turbulent channel flows with ribs mounted on one of the principal walls will be briefly reviewed. Sparrow and Tao [1] employed the naphthalene sublimation technique to determine the mass transfer coefficients in flat rectangular channels of large aspect ratios with rod-type disturbance elements situated adjacent to one of the principal walls of the channel and oriented transversely to the flow direction. The results showed that fully developed Sherwood numbers ($\overline{Sh}$) displayed substantial enhancement compared with the smooth-wall duct, and rate of enhancements up to 140% occurred. Note that the mass transfer coefficients on the rods (metallic rods) were not determined since the rods were not naphthalene-coated surfaces. Drain and Martin [2] performed laser-Doppler velocimetry (LDV) measurements of the fully developed water flow in a rectangular duct with one surface roughened by a periodic rib structure. The rib pitch-to-height ratio (Pr) was fixed at 7.2. The measured data were compared with those predictions from the k–ε–E turbulence model (E stands for the Boussinesq eddy viscosity concept). The mean re-

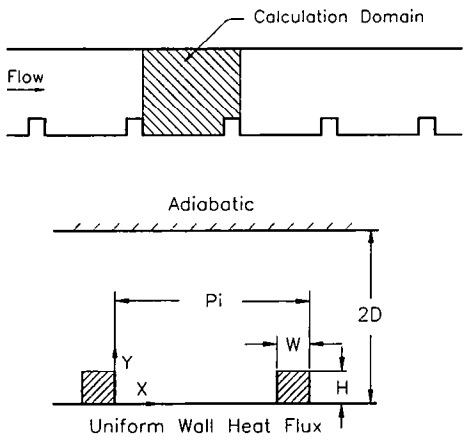

FIG. 1. The ribbed channel geometry and the calculation domain in physical coordinates.

† To whom correspondence should be addressed.

NOMENCLATURE

D	half height of channel [m]
De	hydraulic diameter [m]
H	rib height [m]
k	turbulent kinetic energy [kJ kg^{-1}]
k_f	air conductivity [W m^{-1} K^{-1}]
Nu	local Nusselt number
P	pressure [N m^{-2}]
Pi	rib pitch [m]
PR	rib pitch-to-rib height ratio, Pi/H
Pr	Prandtl number
Q''	heat transfer per unit span [W m^{-1}]
$\dot{q}_w$	local wall heat flux [W m^{-2}]
Re	Reynolds number, $U \cdot De/v$
Sh	Sherwood number
T	local temperature of air [K]
T_b	bulk mean temperature of air [K]
T_w	wall temperature [K]
T^+	dimensionless local air temperature, $\rho c_p u^*(T_w - T)/\dot{q}_w$
T_w^*	dimensionless local wall temperature, $\rho c_p u^*(T_w - T_b)/\dot{q}_w$
t	time [s]
U	axial mean velocity [m s^{-1}]
u	streamwise fluctuation velocity [m s^{-1}]
u^*	friction velocity [m s^{-1}]
V	transverse mean velocity [m s^{-1}]
v	transverse fluctuation velocity [m s^{-1}]
W	rib width [m]
X	axial coordinate
Y	transverse coordinate
Z	spanwise coordinate.

Greek symbols

β	overall pressure gradient
γ	axial gradient of T_w
ε	dissipation rate of turbulence kinetic energy [kJ kg^{-1}]
θ	fluctuation temperature [K]
μ_l	molecular dynamic viscosity [kg m^{-1} s^{-1}]
μ_t	turbulent dynamic viscosity [kg m^{-1} s^{-1}]
ρ	air density [kg m^{-3}]
σ_T, σ_k, σ_ε	turbulent Prandtl numbers of T, k, and ε, respectively.

Subscripts

i, j, k	coordinate indices
REF	reference
s	smooth channel
w	wall.

attachment length was found to be seriously underestimated. Fodemski [3] presented the fluid flow and temperature field for air flowing through a channel with one ribbed heated wall by using an FLOW3D code with the k–ε–E turbulence model. The pitch-to-height ratio of the ribs was kept at a value of 7.13. Qualitative comparison between the simulated [3] and laser holographic interferometry (LHI) measured [4] isotherms was made. Furthermore, the agreement between predicted and measured Nusselt number distributions was found to be unsatisfactory behind the ribs. Lockett and Collins [5] conducted double-exposure holographic interferometry measurement in a channel flow with square and rounded rib-roughness on one wall. The rib pitch-to-height ratio was 7.2. It was found that the heat transfer distribution was Reynolds number-dependent for the rounded rib, but independent for the square rib.

The numerical simulation in the aforementioned technical literature is made of a fixed rib geometry, and contains no information of the effect of rib geometry, such as rib height and rib spacing, on the distributions of local as well as average heat transfer coefficients in a channel with one rib-roughened wall. This provides the motivation for the present work. The k–ε–A turbulence model associated with the preferential dissipation modification [6], which has not been previously applied to solve such a problem, is adopted in the present study. Because of the assumptions made to convert the expressions for Reynolds stresses from differential to algebraic form, the k–ε–A turbulence model is not appropriate to cope with free shear flows where transport effects are significant; however, in internal flows it has been applied successfully and yields results not much different from those obtained by a full Reynolds stress model [7–9], and importantly it is much more economical. The concept used in solving the periodic fully developed laminar flow and heat transfer, described by Patankar *et al.* [10], is employed and extended to a turbulent case in this work. Additionally, the real-time holographic interferometry technique is utilized to measure the time-dependent temperature distribution in the ribbed duct.

The first task in this work is to assess the validity of the numerical approach. The predicted fluid flow and temperature field are tested by previous LDV measurements [2] and present holographic interferometry data, respectively. Then, the regions of the hot spots will be identified by the distribution of the local wall temperature under the uniform wall heat flux (UHF) boundary condition. This has not been reported before. Further, four parameters are varied during the course of the investigation. One is the pitch-to-height ratio of the rib elements, which spans the range from 7.2 to 20. The second parameter, the ratio

of the rib height to duct hydraulic diameter (H/De), has values of 0.067, 0.1, and 0.13. The third is the asymmetric-ribbed wall vs symmetric-ribbed wall. For each configuration, the Reynolds number (Re) is varied from 1.26×10^4 to 6.0×10^4. Finally, in accordance with the numerical results the compact correlation of the heat transfer coefficient is developed in terms of PR, H/De, and Re. This study is one of the first to numerically determine the effect of flow and rib geometry on the heat transfer characteristics from periodic ribbed surfaces in bounded turbulent forced convection.

THEORETICAL TREATMENT

As mentioned previously, since the geometry shown in Fig. 1 has a repeated pattern in the streamwise direction, the calculation can be restricted to a typical module. The concept of a periodic flow regime and a calculation procedure that takes advantage of this phenomenon have been described by Patankar *et al.* [10]; therefore, the explication here will be limited to the important features and the details related to the employment of the turbulence model.

Governing equations

In the periodic fully developed region, the pressure P and the temperature T can be decomposed as $P(X,Y)=-\beta X+\tilde{P}(X,Y)$ and $T(X,Y)=\gamma X+\tilde{T}(X,Y)$. The term βX accounts for the global pressure drop, whereas γX represents the fluid enthalpy rise along the axial direction. The functions $\tilde{P}(X,Y)$ and $\tilde{T}(X,Y)$ identically repeat themselves from pitch to pitch and indicate the local departure of the pressure and the temperature from the linear decay given by $-\beta X$ and the linear increase given by γX, respectively.

The Reynolds-averaged equations for conservation of mass, momentum and energy can be expressed in Cartesian tensor notation as follows:

$$\frac{\partial}{\partial X_i}(\rho U_i)=0 \tag{1}$$

$$\frac{\partial}{\partial X_j}(\rho U_iU_j)=\beta\cdot\delta_{i1}-\frac{\partial\tilde{P}}{\partial X_j}+\frac{\partial}{\partial X_j}\left[\mu_1\left(\frac{\partial U_i}{\partial X_j}+\frac{\partial U_j}{\partial X_i}\right)-\rho\overline{u_iu_j}\right] \tag{2}$$

$$\frac{\partial}{\partial X_i}(\rho U_i\tilde{T})=\frac{\partial}{\partial X_i}\left[\frac{\mu_1}{Pr}\left(\frac{\partial\tilde{T}}{\partial X_i}\right)-\rho\overline{u_i\theta}\right]-\rho\cdot U_i\cdot\gamma\cdot\delta_{i1}. \tag{3}$$

The turbulence model adopted here is based on solving transport equations for the Reynolds stresses and Reynolds heat flux. The algebraic Reynolds stress and Reynolds heat flux transport equations can be written in tensor notation form as

$$\frac{\overline{u_iu_j}}{k}\cdot(P_k-\varepsilon)=P_{ij}-\tfrac{2}{3}\delta_{ij}\cdot\varepsilon-C_{A1}\cdot\frac{\varepsilon}{k}(\overline{u_iu_j}-\tfrac{2}{3}\delta_{ij}\cdot k)-C_{A2}(P_{ij}-\tfrac{2}{3}\delta_{ij}P_k) \tag{4}$$

$$\frac{\overline{u_i\theta}}{2k}\cdot(P_k-\varepsilon)=-\left(\overline{u_iu_m}\cdot\frac{\partial T}{\partial X_m}+\overline{u_m\theta}\cdot\frac{\partial U_i}{\partial X_m}\right)-C_{T1}\cdot\frac{\varepsilon}{k}\cdot\overline{u_i\theta}+C_{T2}\cdot\overline{u_m\theta}\cdot\frac{\partial U_i}{\partial X_m} \tag{5}$$

which can be further reduced to

$$\frac{\overline{u_iu_j}}{k}=\tfrac{2}{3}\delta_{ij}+\frac{(1-C_{A2})\left(\dfrac{P_{ij}}{\varepsilon}-\tfrac{2}{3}\delta_{ij}\dfrac{P_k}{\varepsilon}\right)}{C_{A1}+\dfrac{P_k}{\varepsilon}-1} \tag{6}$$

$$-\frac{\overline{u_i\theta}}{k}=\frac{\overline{u_iu_m}\cdot\dfrac{\partial T}{\partial X_m}+(1-C_{T2})\left(\overline{u_m\theta}\cdot\dfrac{\partial U_i}{\partial X_m}\right)}{\varepsilon\left[C_{T1}+\dfrac{1}{2}\left(\dfrac{P_k}{\varepsilon}-1\right)\right]} \tag{7}$$

where $P_k=\overline{u_mu_n}\cdot(\partial U_m/\partial X_n)$ and $P_{ij}=-[\overline{u_iu_m}\cdot(\partial U_j/\partial X_m)+\overline{u_ju_m}\cdot(\partial U_i/\partial X_m)]$.

Furthermore, the local effect of a rigid solid wall on the pressure strain correlation can be expressed through modification of the constants C_{A1} and C_{A2} with the following relationships [11], respectively:

$$\tilde{C}_{A1}=C_{A1}-0.125\frac{k^{3/2}}{\varepsilon z_p} \tag{8}$$

$$\tilde{C}_{A2}=C_{A2}-0.015\frac{k^{3/2}}{\varepsilon z_p} \tag{9}$$

where z_p is the distance to the solid wall.

The turbulent kinetic energy k and its dissipation rate ε appearing in the above equations can be obtained by solving the k- and ε-equation, which are expressed in the following way:

$$\rho U_j\frac{\partial k}{\partial X_j}=\frac{\partial}{\partial X_j}\left[\left(\mu_1+\frac{\mu_1}{\sigma_k}\right)\cdot\frac{\partial k}{\partial X_j}\right]-\rho\overline{u_iu_j}\cdot\frac{\partial U_i}{\partial X_j}-\rho\varepsilon \tag{10}$$

$$\rho U_j\frac{\partial\varepsilon}{\partial X_j}=\frac{\partial}{\partial X_j}\left[\left(\mu_1+\frac{\mu_1}{\sigma_\varepsilon}\right)\cdot\frac{\partial\varepsilon}{\partial X_j}\right]-C_1\cdot\frac{\varepsilon}{k}\cdot\rho\overline{u_iu_j}\cdot\frac{\partial U_i}{\partial X_j}-C_2\cdot\rho\cdot\frac{\varepsilon^2}{k}. \tag{11}$$

Equations (4)–(11) form the k–ε algebraic stress model (abbreviated as k–ε–A). For strongly accelerated flows, Hanjalic and Launder [12] observed that the normal stresses are more effective than shear stresses in the promotion of the dissipation of turbulence energy. With the intention also of improving the k–ε–A model when applied to recirculating flow, Leschziner and Rodi [6] retained the basic idea of preferential-normal-stress treatment and proposed

Table 1. Constants in the k–ε–A PDM model

C_1	C_2	σ_k	σ_ε	σ_T	C_{A1}	C_{A2}	C_{T1}	C_{T2}	C_μ	C'_1	C''_1
1.44	1.92	1.0	1.3	0.9	2.3	0.4	3.2	0.5	0.09	2.24	0.8

the replacement of the 'production-of-dissipation' term $P_\varepsilon = C_1 \cdot \varepsilon \cdot (-\rho\overline{u_i u_j}) \cdot (\partial U_i/\partial X_j)/k$ in equation (11) by the expression

$$P_\varepsilon = \frac{\varepsilon}{k}\left[C'_1 \cdot \left(-\rho\overline{u_i u_j} \cdot \frac{\partial U_i}{\partial X_j}\right) - C''_1 \cdot \mu_t S_{ns}^2\right] \quad (12)$$

where S_{ns} is the shear strain along the streamline and is determined by the transformation of a rate-of-strain tensor in a rectangular coordinate system to a rotated system. The above 'preferential dissipation modification' (PDM) to the k–ε–A model will be referred to as the k–ε–A PDM model in the present paper. The empirical constants in the above equations are given in Table 1 [13].

Boundary conditions

The periodic behavior at the inlet and outlet of the flow leads to the boundary conditions given by

$$U(0, Y) = U(Pi, Y), \quad V(0, Y) = V(Pi, Y)$$
$$k(0, Y) = k(Pi, Y), \quad \varepsilon(0, Y) = \varepsilon(Pi, Y)$$
$$\tilde{T}(0, Y) = \tilde{T}(Pi, Y), \quad \tilde{P}(0, Y) = \tilde{P}(Pi, Y).$$

The boundary conditions do not involve any specification of inflow velocities; therefore, the flow rate through the channel cannot be directly prescribed. On the other hand, the pressure gradient β must be specified for the solution of equations (1)–(3). For any given value of β, there will be a corresponding value of flow rate in the channel. In a numerical computation, this makes it possible to iteratively adjust the pressure gradient so that the converged solution is obtained for a desired flow rate or Reynolds number.

At the wall boundaries, momentum, energy, and turbulence kinetic energy are evaluated from the 'law of the wall', while the energy dissipation rate is determined from the 'local equilibrium condition' which gives linear variation of the turbulence length scale from the solid wall.

Numerical method

The finite difference scheme SCSUDS (Smoothed hybrid Central/Skew Upstream Difference Scheme) [14] is used to reduce numerical diffusion resulting from the existence of large cross-flow gradients and the obliquity of the flow to the grid lines [15], which did occur in the present study. As for handling the pressure–velocity coupling arising in the implicitly discretized fluid flow equations, the PISO (Pressure Implicit with Splitting of Operators) [16] method is utilized in this paper for a stable and faster convergence [17]. The tolerance of the nondimensionalized residual is typically 0.005. k and ε are also solved line by line simultaneously with the mean velocity distribution.

All computations are performed on a 50×50 grid. The grid is nonuniform and denser near solid surfaces and in the separated shear layer. In both places, steeper gradients of dependent variables are expected. Additional runs for coarser (30×30 and 40×40) and finer (75×75) meshes are taken for a check of grid independence. The parameters used to check the grid independence are axial velocity profile, temperature profile, and local Nusselt number distribution. A comparison of the results of the two grid sizes, 50×50 and 75×75, shows that the maximum changes in the axial velocity/temperature profiles are about 0.8%/1.3% and 0.9%/1.8% for $PR = 10$ and 20, respectively, at Re and H/De values of 12 600 and 0.1. Computations for $PR = 7.2$, $Re = 30\,000$, and $H/De = 0.1$ were also conducted and the results indicate a maximum change of 1.5% in Nusselt number distribution between the solutions of 50×50 and 75×75 grids. These changes are so small that the accuracy of the solutions on a 50×50 grid is deemed satisfactory. The corresponding CPU time on a CDC-CYBER 180/840 computer is about 8 s for each iteration, and typically it takes 2000–3000 iterations to reach convergence.

EXPERIMENTAL APPARATUS AND PROCEDURE

The experimental apparatus, shown in Fig. 2, consists of an air flow system with a test section and an optical system. Room air is drawn through a settling

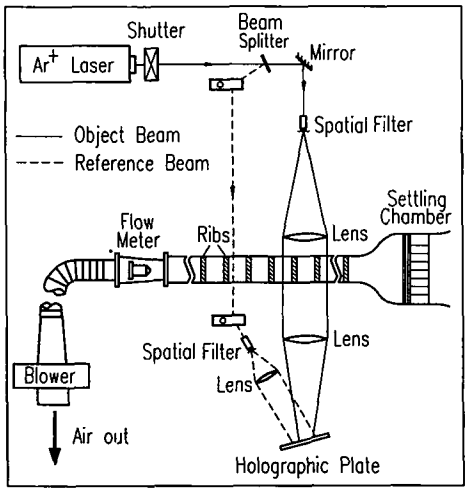

FIG. 2. Schematic drawing of the overall experimental system.

chamber with a honeycomb-type flow straightener, four screens and a 10:1 contraction, into the test section by a 3 hp blower at the downstream end. After traversing the test section, the air subsequently flows through a flow straightener, a rotameter, and a bellows, and is finally exhausted by the blower.

The test section length in the flow direction is 1200 mm and has a cross-sectional area of 160×40 mm^2 (X–Y plane), i.e. a cross-sectional aspect ratio of 4:1. The bottom wall of this channel, consisting of an aluminum plate, is covered by square ribs of size 8×8 mm^2. A thermally-conducting epoxy cement is served to ensure good contact between the plate and ribs. The thermal resistance associated with the thin layer of epoxy cement (less than 0.13 mm) at the interface is negligible [18]. The aluminum plate is highly polished to minimize radiation losses. A 7.5 Ω thermal foil of 0.18 mm thickness is adhered uniformly at the bottom side surface of the aluminum plate. The thermal foil can be controlled by a transformer, hence a controllable uniform heat flux for the thermal foil is obtained. The maximum heat loss from the back side of the aluminum plate is estimated to be less than 12%. The top wall of the test section is made of a bakelite plate and an insulating material to prevent heat loss; therefore, it does not participate in the heat transfer process. The side walls of the entire test duct are made of Plexiglas plates to provide optical access for interferometry measurements.

The technique of real-time holographic interferometry is used to measure the temperature distribution of air flow in the ribbed channel. The overall arrangement of the holographic interferometer is illustrated in Fig. 2. The laser used in this work is a 3 W argon-ion (514.5 nm) Spectra-Physic Model 2000, the high power being required for subsequent real-time work. The photographic emulsion 8E56 made by Agfa-Gevaert Ltd is found to be a suitable recording material for combining a good compromise between light sensitivity and resolution. All experiments are conducted using the adjustment of an infinite fringe field and, therefore, the interference fringes represent the isotherms in the fluid. Through a CCD camera which allows 512×512 pixel resolution with 256 grey levels per pixel, the instantaneous interference field is digitized and recorded on a VHS videocassette recorder for storage and further image processing.

In order to compare with the periodic results of the present prediction, the holograms are taken for the region of $12.0 \leqslant X/De \leqslant 14.3$, where both the hydrodynamic and the thermal fully developed conditions are attained. In practice, the onset of the periodic fully developed region occurs about five hydraulic diameters downstream of the duct inlet [19]. It is necessary to ensure that the temperature distributions along the test section width in the flow field are two-dimensional because the holographic interferometry technique used in this study is based on the integral of the change in refractive index. According to Bradshow's suggestion [20], the channel aspect ratio should be at least 10:1 for a reasonable two-dimensionality approximation. However, the significant errors usually encountered in the interferometric experiments are not only due to the end effect which is caused by deviation from two-dimensionality of the actual temperature field, but also due to the refraction effect. The refraction effect occurs when there is a density gradient normal to the light beam causing the beam to bend, and the resulting error increases with increasing disturbed length (Z direction). Thus if an experimental apparatus is designed to minimize the end-effect error (increasing the optical path length) the refraction-effect error might be large, and vice versa. The aspect ratio of the channel used in this work is 4:1 for a reasonable combination of the end-effect and refraction-effect errors. The same aspect ratio is employed in Walklate [21] for the study of two-dimensional thermal boundary layers and in Lockett and Collins [5] for the study of rib-roughened channel flows. Nevertheless, the two-dimensionality of the spanwise temperature profile of the flow field is checked by the thermocouple probing in this study, and the scatter in the spanwise direction was less than 6% of the channel spanwise average temperature. The error in estimating the temperature field of the channel flow in this work is within ±9%, and the detailed error and interferogram analyses are given in Liou and Hwang [22] for a channel with periodic ribs on two principal walls.

RESULTS AND DISCUSSION

Comparison with experimental results

Figures 3(a) and (b) present a comparison of the calculated and measured [2] mean axial velocity and turbulent kinetic energy profiles at selected axial stations for $PR = 7.2$, $H/De = 0.1$, and $Re = 3.74 \times 10^4$. The measured results were obtained for turbulent water flow in a rectangular channel with a cross-sectional aspect ratio of 8:1 and with one surface roughened by square ribs of size 5×5 mm^2 by using LDV. The measurements show that reattachment of the flow to the channel wall between the ribs occurs at about $X = 4.32H$, whereas theory predicts it to be at $X = 4.01H$. Thus, according to the present calculation with the k–ε–A PDM turbulence model, a 7.2% underprediction of the reattachment length is found. The underprediction is partly due to the near-wall treatment of the wall function, which is only valid for the normal boundary layers, and partly due to the uncertainty in the experimentally measured reattachment length. As for the turbulent kinetic energy, the major discrepancies occur in the rib-top region where local peak turbulent kinetic energy appears. The discrepancies may be due to the inadequacy of the basic assumption $\overline{u_i u_j}/k$ = constant made in the k–ε–A model in the rib-top region, where $\overline{u_i u_j}/k$ varies in the range of 0.1–0.4 [23].

Typical examples of real-time interferograms taken from the temperature fields of square-rib geometry

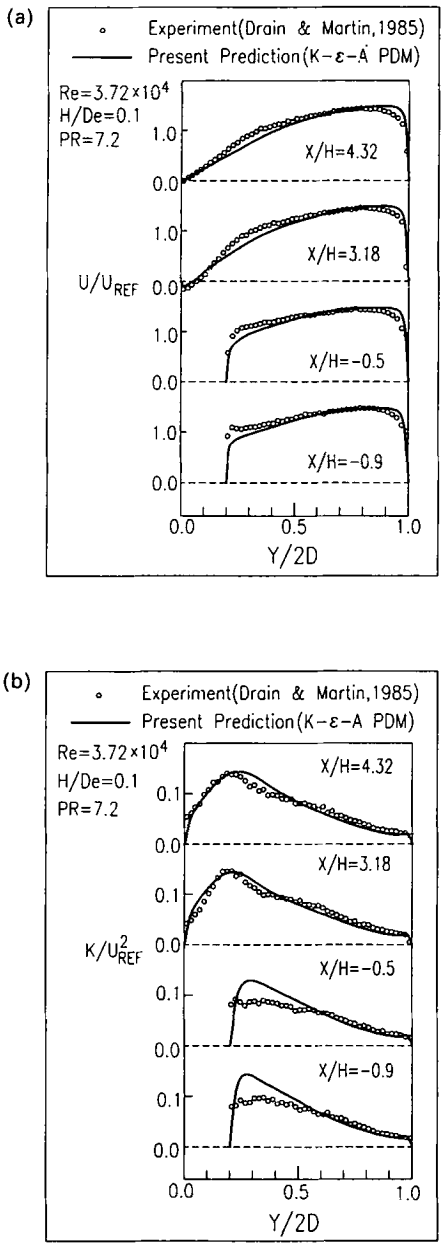

FIG. 3. (a) Comparison of predicted and measured streamwise mean velocity profiles at selected axial stations. (b) Comparison of predicted and measured turbulent kinetic energy profiles at selected axial stations.

are shown in Figs. 4(a) and (b) for $PR = 7.2$, $H/De = 0.1$ and $Re = 1.26 \times 10^4$. The measurements were taken at intervals of 0.017 s. The measured and computed nondimensional temperature profiles of the flow field at selected axial stations are depicted in Fig. 5. The axial stations are in the positions cutting across the rib top ($X/H = -0.5$), the recirculation zone ($X/H = 2.0$), and the redeveloping zone ($X/H = 5.0$). The different symbols represent temperature distributions at different instants calculated from the corresponding interferograms, whereas the dotted lines are the mean values predicted by the k–ε–A PDM model. It is interesting to note that the variance of the measured temperature is as high as 20% of the mean value in the core flow region; however, in the regions close to the ribs and channel walls the variance is very small, about 3% of the mean value. An explanation for this phenomenon is that the turbulence length scale in the core flow region is of the same order as the optical path length across the test section, thus a disturbance of the large scale motion will cause a large fluctuation in temperature. However, the turbulence eddies near the ribs and walls are small compared with the total disturbed optical path. Therefore, the line integral measurement of the temperature field is nearly independent of time. A similar finding was reported by Walklate [21] for the study of two-dimensional thermal boundary layers. A comparison between the time-averaged temperature profile predicted by the k–ε–A PDM model and the instantaneous temperature profile measured by holographic interferometry reveals a deviation as high as 25% of the predicted mean value. However, a comparison between the predicted mean value and the calculated one from 50 instantaneous interferograms is also useful, and as a result, a difference of 6% is found.

Generally speaking, the agreement of the computational and experimental values in mean velocity, turbulent kinetic energy and temperature is reasonably good in this work. The encouraging ability of the present procedures to predict fluid-dynamic as well as thermo-transport phenomena lends strong support to the evaluation of the effectiveness of heat transfer enhancement of periodic ribs mounted on heated channel walls.

Local wall temperature distribution

Figure 6 shows the distribution of the calculated local dimensionless surface temperature difference (T_w^*) of the periodic fully developed ribbed duct flow along the length of the duct for $PR = 7.2$, $H/De = 0.1$, and $Re = 1.26 \times 10^4$. The local T_w^* of the smooth duct (dashed line) is also included for comparison. To serve the interest of clarity, the rib perimeter is expanded linearly along the abscissa of the figure. The figure illustrates how the presence of the ribs permits the redistribution of the local wall temperature with the uniform wall heat flux (UHF) boundary condition. In fact, the wall temperature rises linearly along the length of the duct, and the wall-to-fluid temperature difference attains a constant value for a conventional smooth-duct flow with the UHF boundary condition at a sufficient distance from the duct inlet. Thus, the local dimensionless wall-to-fluid temperature difference T_w^* (dashed line) becomes constant for the fully developed smooth duct flow with the UHF boundary condition. As shown in Fig. 6, the average value of T_w^* (center line) of the ribbed duct flow is lower than that of the smooth one (dashed line). This indicates that the overall heat transfer augmentation is achieved by reducing the wall-to-fluid temperature difference when the periodic ribs are applied to the wall. In

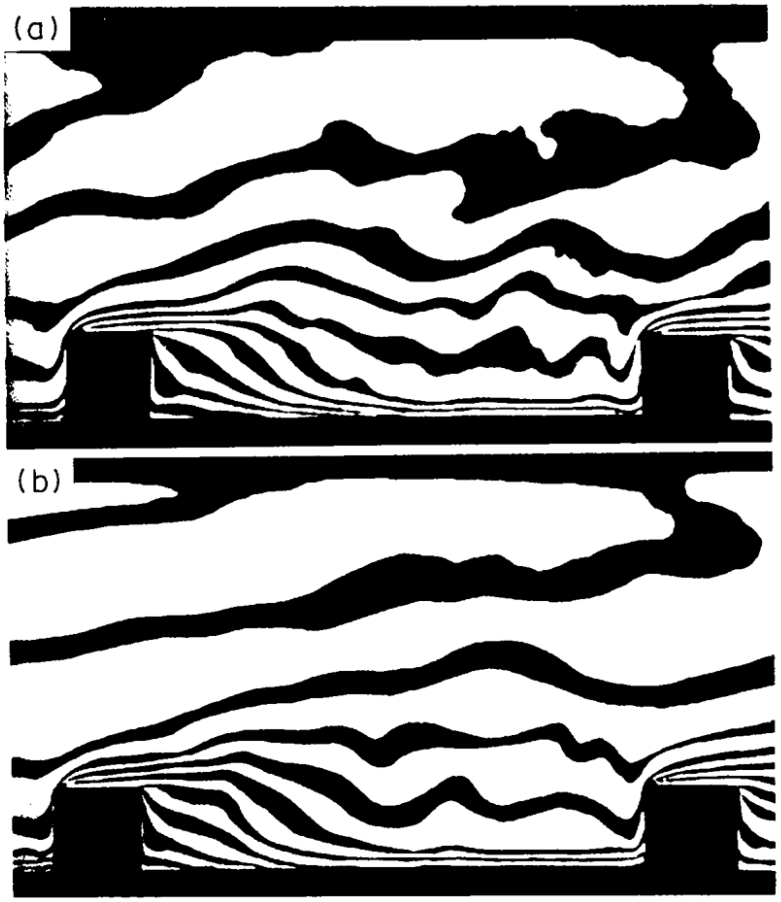

FIG. 4. Typical examples of the holographic interferograms of the full-field temperature distributions: (a) $Re = 1.26 \times 10^4$, $H/De = 0.1$, $PR = 7.2$ and $t = 0$ s; (b) $Re = 1.26 \times 10^4$, $H/De = 0.1$, $PR = 7.2$ and $t = 0.017$ s.

contrast to the UHF boundary condition, the uniform wall temperature (UWT) boundary condition is usually adopted in conventional mass transfer experiments, e.g. the naphthalene sublimation method [1]; the heat (mass) transfer augmentation is reflected in the increase of the heat (mass) transfer rate. With regard to the distribution of T_w^* of the ribbed duct flow, the lowest value of T_w^* occurs on the rib top, where the influence of high velocities and turbulent kinetic energies is most pronounced. This produces a more effective heat transfer coefficient in this region. On the other hand, the maximum value of T_w^* appears in the vicinity of the corner 0, where the value of T_w^* is very much higher than that of the smooth one. The uneven wall temperature distribution is due to the stagnant fluid at these locations, and will cause material structure failure. This suggests the existence of the hot spot around the concave corner (0).

Local Nusselt number distribution

Since the temperatures have been measured by LHI, the local Nusselt numbers can be determined from the temperature profiles. The data reduction of the measured Nu based on the bulk mean temperature is shown in detail in Liou and Hwang [22]. In numerical predictions, the local Nusselt number is defined by

$$Nu = \dot{q}_w \cdot De/[k_f \cdot (T_w - T_b)]. \quad (13)$$

The quantity T_b appearing in equation (13) is the local bulk mean temperature of the air, which is defined as

$$T_b = \int_0^{2D} T \cdot |U| \cdot Y \cdot dY \Big/ \int_0^{2D} |U| \cdot Y \cdot dY \quad (14)$$

where the absolute values of U are used so that the integral is properly calculated in regions of reverse flow. Note that the local bulk mean temperature used in computing the local Nusselt number along the upstream and downstream vertical faces of the rib is the value of T_b at $X/H = -1$ and 0, respectively.

Figures 7–11 show the distributions of the local heat transfer coefficient on the ribbed wall for periodically fully developed flow. In all subsequent similar plots, the mean flow direction is from left to right. Because of the use of participating ribs, these maps display results not only between ribs, but also ribs themselves. The results are expressed in the form of the Nusselt number ratio, $Nu/\bar{Nu}_s = Nu/(0.023Re^{0.8}\,Pr^{0.4})$, which

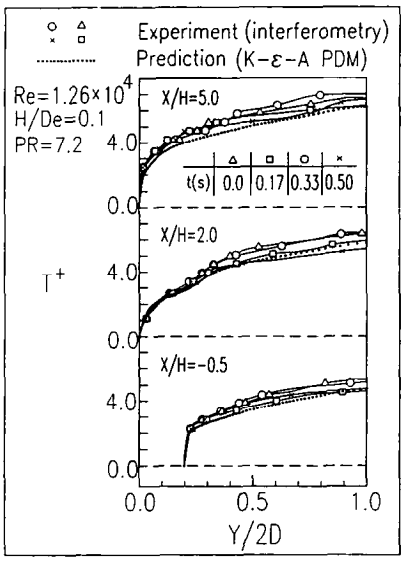

FIG. 5. Measured and computed temperature profiles at selected axial stations.

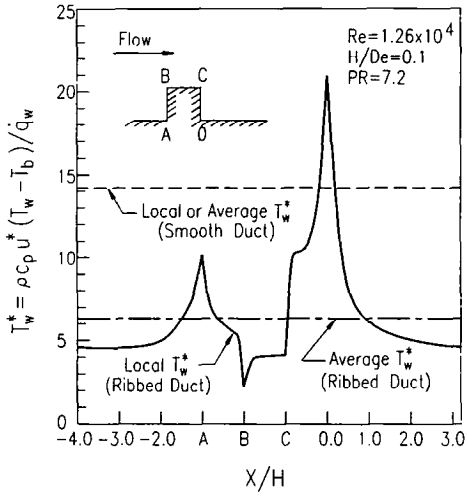

FIG. 6. Local dimensionless wall temperature distribution.

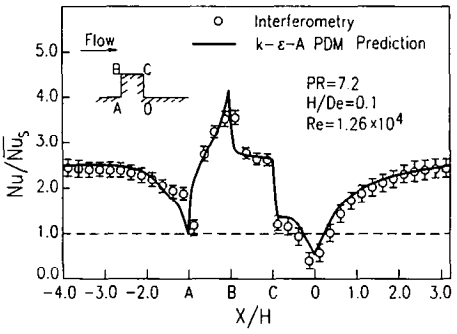

FIG. 7. Comparison of measured and predicted local Nusselt number distributions.

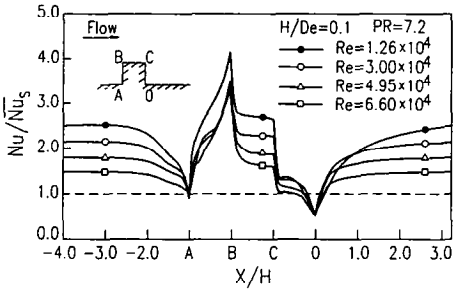

FIG. 8. Effect of Reynolds number on local Nusselt number distributions.

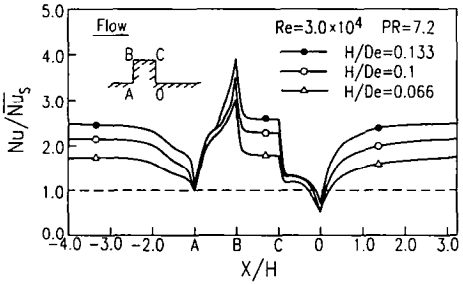

FIG. 9. Effect of rib height on local Nusselt number distributions.

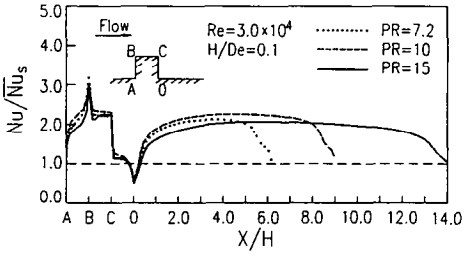

FIG. 10. Effect of rib spacing on local Nusselt number distributions.

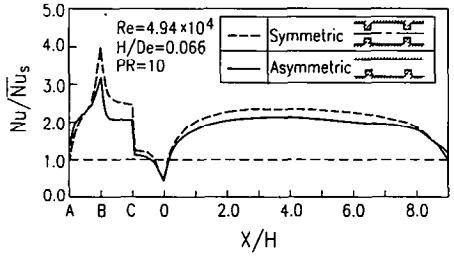

FIG. 11. Comparison of local Nusselt number distributions for symmetric and asymmetric ribbed ducts.

is normalized by the Nusselt number for fully developed turbulent flow in smooth circular tubes (Dittus–Boelter correlation). A comparison of the distributions of predicted and measured local heat transfer coefficients is shown in Fig. 7 for $PR = 7.2$, $Re = 12\,600$, and $H/De = 0.1$. In general, the k–ε–A PDM model predictions are in good agreement with the LHI measurements. Typical variations of the calculated local heat transfer coefficient on the ribbed wall under the effects of various parameters are shown in Figs. 8–11. An insight into these figures reveals a familiar trend. That is, initially the Nusselt number ratio increases fairly rapidly along the front surface of the rib and reaches a local maximum near the upstream protruding corner (B) at which the flow turns, the isotherm lines are packed closely (Fig. 4) and the lowest local wall temperature appears (Fig. 6). Then it decreases gradually until the flow passes over the end of the top surface of the rib because the secondary thermal boundary layer on the rib top surface becomes thicker. Subsequently, the Nusselt number ratio decreases along the rear face of the rib because of the recirculation flow, and then increases, although not significantly, up to another local maximum around the reattachment region in the inter-rib. Finally, it decreases gradually until the next rib is encountered. It is interesting to note that the heat transfer around the corner behind the rib is relatively poor ($Nu/\overline{Nu}_s < 1$).

Typical results to illustrate the effect of the Reynolds number on the local Nusselt number ratio distribution of the ribbed channel flows are shown in Fig. 8 for $PR = 7.2$ and $H/De = 0.1$. The velocity increases with increasing Reynolds number, which results in a heat transfer rate increase. However, the effect of the Reynolds number on the heat transfer rate of a ribbed duct is not as significant as that of a smooth one. Therefore, the Nusselt number ratio decreases with the increase of the Reynolds number. Figure 9 shows the effect of dimensionless rib height, H/De, on the local Nusselt number ratio distributions. In this plot, PR and Re are kept at values of 7.2 and 3.0×10^4, respectively. It is seen in Fig. 9 that the local Nusselt number ratio on the rib top and inter-rib increases with the increase of the rib height because of increasing local flow acceleration and turbulence intensity. However, the Nusselt number ratio does not seem to be affected by the rib height in the region of the rear face of the rib since the recirculating fluids behind the rib are nearly stagnant for different heights [22]. Typical results showing the effect of rib spacing on the local heat transfer coefficients are plotted in Fig. 10 for $Re = 3.0 \times 10^4$ and $H/De = 0.1$. The case of $PR = 7.2$ enhances about the same amount of heat transfer as the case of $PR = 10$; however, the level of enhancement is lower in the case of $PR = 15$. The reasons are the combined effects of flow acceleration and turbulence intensity, and will be demonstrated later.

A comparison of the effect on heat transfer coefficients between the mechanism of symmetric ribs arranged on two opposite walls and that of asymmetric ribs arranged on one wall is also interesting and is shown in Fig. 11 for $PR = 10$, $Re = 4.94 \times 10^4$ and $H/De = 0.066$. It is obvious from this figure that the heat transfer coefficients of the symmetric-rib case are higher than those of the asymmetric-rib case. The local conditions of higher gap velocity on the rib top for the symmetric-rib case provide an environment for higher $Nu/\overline{Nu}_s$. The increase of turbulence intensity caused by the presence of the ribs on the opposite wall for the symmetric-rib case, which did not participate in the heat transfer process, results in the increase of the heat transfer coefficients in the inter-rib region.

Average Nusselt number and correlation

Figure 12 gives the average values of Nusselt number ratios of the ribbed channel as a function of Reynolds number for several combinations of the geometric parameters PR and H/De. The plotted symbols indicate the actual results of the computations and the solid lines passing through these symbols are least-square fits. It is observed from this figure that heat transfer augmentation ($Nu/\overline{Nu}_s > 1$) is achieved in all of the investigated cases. The amount of increase of the average heat transfer coefficients varied between 50 and 140% as compared with the smooth-duct results for the range of Reynolds number, dimensionless rib spacing, and dimensionless rib height investigated. A comparison is also made in Fig. 12 between the numerical results of this investigation and the experimental work (cross symbols) of Lockett and Collins [5] for $PR = 7.2$ and $H/De = 0.066$. The comparison shows good agreement (within an average difference of 11%). With the values illustrated in Fig. 12, the average Nusselt number is further correlated in terms of the rib and flow parameters PR, H/De, and Re as follows:

$$\overline{Nu} = [0.941 + 0.308(PR/10) - 0.152(PR/10)^2] \cdot (H/De)^{0.402} \cdot Re^{0.571}. \quad (15)$$

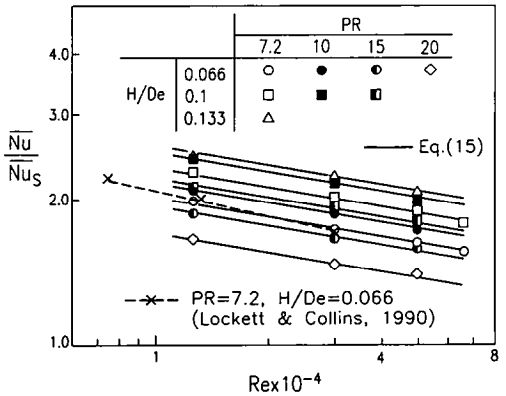

FIG. 12. Fully developed Nusselt number ratios vs Reynolds number.

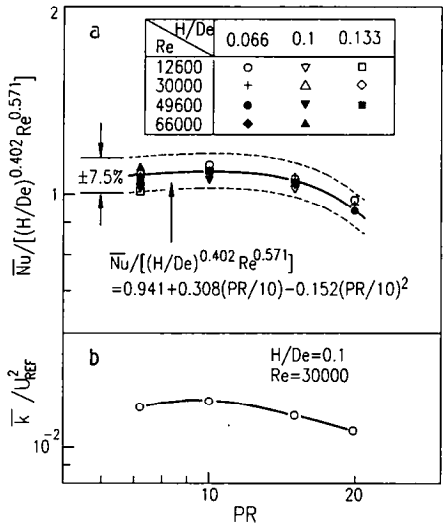

FIG. 13. (a) Correlation of $\overline{Nu}$ with Re, H/De and PR. (b) Turbulent kinetic energy vs PR.

Comparing the above equation with numerical results, as shown in Fig. 13, the maximum relative error is 7.5% and the mean relative error is 2.5%. The Reynolds number dependence ($Re^{0.571}$) of the ribbed duct flow revealed in the above correlation is less than that of the smooth one ($Re^{0.8}$). This is reasonable because in the rib-duct case part of the mean-flow energy used for convection heat transfer has been transferred into turbulent kinetic energy, which subsequently enhances the heat transfer rate through enhanced turbulence transport. Surprisingly, the average Nusselt number does not, as one may expect, decrease monotonously with increasing PR, but slightly increases with PR changes from 7.2 to 10 and then decreases with increasing PR. The maximum value is around $PR = 10$ for the values of Re and H/De investigated. The reason is that although the increase of flow acceleration in a densely ribbed channel ($PR = 7.2$) is significant, the recirculation regions downstream of the rib, which do not contribute much to heat transfer, proportionally become a larger fraction of the total heat transfer area, and the gain in the average heat transfer coefficient (on a total heat transfer area basis) will suffer. It is interesting to note that the results obtained by Han *et al.* [24] showed that the heat transfer coefficients for $PR = 7.5$ are slightly higher than those for $PR = 10$. This is reasonable because the average heat transfer coefficients in their work are based on the projective area and the aforementioned effect of the rib-rear-facing heat transfer disappears. Also, it can be found that the average heat transfer on the rib surfaces (front-facing, top, and rear-facing; $\overline{Nu}_{ABCO}$) is in general comparable to that on the inter-rib surfaces ($\overline{Nu}_{OA}$) for $PR = 10$ and $PR = 7.2$ reported here. Thus, the average Nusselt number based on the total heat transfer area is not affected by the frequency of flow acceleration, which increases with decreasing PR. Hence, the heat transfer enhancement may be dominated by turbulent transport. Figure 13 shows a similar trend of the distributions between the average turbulent kinetic energy

$$\left(\bar{k} = \int_0^{P_i} k \, dx/Pi\right)$$

and the average Nusselt number. According to the above results, it is concluded that the reduction of rib pitch from $PR = 20$ to 10 causes the increase of both the average turbulent kinetic energy (Fig. 13) and the flow acceleration. Thus, the average Nusselt number increases with decreasing PR in the range of $PR = 10$ and 20. As the rib pitch reduces continuously from $PR = 10$ to 7.2, the average turbulence intensity decreases, although the flow acceleration still increases with the decrease of rib pitch (Fig. 13), which causes a decrease of the average Nusselt number. Consequently, the existence of an optimum pitch represents the situation in which the effects of acceleration and turbulence intensity are mixed properly.

SUMMARY AND CONCLUSIONS

Both numerical and experimental studies have been made for the periodic fully developed turbulent flow field and heat transfer in a channel with one surface roughened by ribs. The computation is confined within a unit module of the duct with a resultant economy of computational effort. In experiments, the time-dependent temperature profiles of the ribbed duct flows were obtained by using real-time holographic interferometry. In general, the predictions with the k–ε–A PDM turbulence mode, SCSUDS finite difference scheme, and PISO algorithm adequately simulate the characteristics of both flow and temperature fields. The key conclusions are described as follows.

(1) With the uniform wall heat flux boundary condition, the rib geometry redistributes the local dimensionless wall temperature and has the advantage of reducing the average dimensionless wall temperature because of the flow acceleration and the increase of turbulence intensity. However, the local hot spots around the corner behind the ribs, which are caused by the stagnant fluid at these locations, are disadvantageous to the material structure.

(2) The effects of the flow and geometry parameters on the heat transfer coefficients are discussed. The heat transfer correlation is developed in terms of Reynolds number, rib height, and rib spacing.

(3) The flow acceleration and the turbulence intensity are two major factors influencing the heat transfer coefficient and are mixed mutually and properly for $PR = 10$, which will result in the maximum value of average heat transfer coefficient on a total heat transfer area basis.

Acknowledgement—Support for this work was provided by the National Science Council of the Republic of China under contract NSC 79-0401-E007-07.

REFERENCES

1. E. M. Sparrow and W. Q. Tao, Enhanced heat transfer in a flat rectangular duct with streamwise-periodic disturbances at one principal wall, *Trans. ASME J. Heat Transfer* **105,** 851–861 (1983).
2. L. E. Drain and S. Martin, Two-component velocity measurements of turbulent flow in a ribbed-wall flow channel, *Int. Conf. on Laser Anenometry—Advances and Application*, Manchester, U.K., pp. 99–112 (1985).
3. T. R. Fodemski, The simulation of flow and heat transfer in channels with ribbed surface, *2nd Int. Symp. on Transport Phenomena in Turbulent Flows*, Tokyo, Japan (1987).
4. J. F. Lockett and M. W. Collins, Holographic interferometry and its applications to turbulent convective heat transfer, *Int. J. Opt. Sensors* **1,** 191–244 (1986).
5. J. F. Lockett and M. W. Collins, Holographic interferometry applied to rib-roughness heat transfer in turbulent flow, *Int. J. Heat Mass Transfer* **33,** 2439–2449 (1990).
6. M. A. Leschziner and W. Rodi, Calculation of annular and twin parallel jets using various discretization schemes and turbulence-model variations, *Trans. ASME J. Fluid Engng* **103,** 352–360 (1981).
7. W. Rodi, *Turbulence Models and Their Applications in Hydraulics*. McGraw-Hill, New York (1984).
8. R. H. Pletcher, Progress in turbulent forced convection, *Trans. ASME J. Heat Transfer* **110,** 1129–1144 (1988).
9. S. Fu, P. G. Huang, B. E. Launder and M. A. Leschziner, A comparison of axisymmetric turbulent shear flows with and without swirl, *Trans. ASME J. Fluids Engng* **110,** 216–221 (1988).
10. S. V. Patankar, C. H. Liu and E. M. Sparrow, Fully developed flow and heat transfer in ducts having streamwise-periodic variations of cross-sectional area, *Trans. ASME J. Heat Transfer* **99,** 180–186 (1977).
11. B. E. Launder and D. B. Spalding, The numerical computation of turbulent flow. *Comput. Meth. Appl. Mech. Engng* **3,** 269–289 (1974).
12. K. Hanjalic and B. E. Launder, Preferential spectral transport by irrotational straining, *Turbulent Boundary Layers*, pp. 101–110. ASME (1979).
13. C. J. Chen, *Prediction of Turbulent Flows*. The University of Iowa, Iowa City (1986).
14. T. M. Liou, Y. Chang and D. W. Hwang, Experimental and computational study of turbulent flows in a channel with two pairs of turbulence promoters in tandem, *Trans. ASME J. Fluid Engng* **112,** 302–310 (1990).
15. G. D. Raithby, Skew upstream difference schemes for problems involving fluid flow, *Comput. Meth. Appl. Mech. Engng* **9,** 153–164 (1976).
16. R. I. Issa, Solution of implicitly discretized fluid flow equations by operator-splitting, *J. Comput. Phys.* **62,** 40–85 (1986).
17. D. S. Jang, R. Jetli and S. Acharya, Comparison of PISO, SIMPLER, and SIMPLE-C algorithms for the treatment of the pressure–velocity coupling in steady flow problem, *Numer. Heat Transfer* **10,** 209–228 (1986).
18. J. C. Han, Heat transfer and friction in channels with two opposite rib-roughened walls, *Trans. ASME J. Heat Transfer* **106,** 774–781 (1984).
19. J. C. Han, Heat transfer and friction characteristics in rectangular channels with rib turbulators, *Trans. ASME J. Heat Transfer* **110,** 321–328 (1988).
20. P. Bradshow and F. Y. F. Wang, The reattachment and relaxation of a turbulent shear layer, *J. Fluid Mech.* **52,** 113–135 (1972).
21. P. J. Walklate, A two wavelength holographic technique for the study of two-dimensional thermal boundary layers, *Int. J. Heat Mass Transfer* **24,** 1051–1057 (1980).
22. T. M. Liou and J. J. Hwang, Turbulent heat transfer augmentation and friction in periodic fully developed channel flows, *Trans. ASME J. Heat Transfer* **114,** 56–64 (1992).
23. Y. Chang, Experimental analysis of turbulent flows in a rectangular duct with repeated square-rib pairs, Master's Thesis, Department of Power Mechanical Engineering, National Tsing Hua University, Hsinchu, Taiwan, R.O.C. (1990).
24. J. C. Han, J. S. Park and C. K. Lei, Augmented heat transfer in rectangular channel of narrow aspect ratios with rib turbulators, *Int. J. Heat Mass Transfer* **32,** 1619–1630 (1989).